materials

MDPI

Article

Static and Resonant Properties and Magnetic Phase Diagram of $LiMn_2TeO_6$

Tatyana Vasilchikova [1,2], Evgeniya Vavilova [3], Timur Salikhov [3], Vladimir Nalbandyan [4], Shanu Dengre [5], Rajib Sarkar [5], Hans-Henning Klauss [5] and Alexander Vasiliev [1,2,*]

1 Low Temperature Physics and Superconductivity Department, Lomonosov Moscow State University, 119991 Moscow, Russia
2 Functional Quantum Materials Laboratory, National University of Science and Technology "MISiS", 119049 Moscow, Russia
3 Zavoisky Physical-Technical Institute, FRC Kazan Scientific Center of RAS, 420029 Kazan, Russia
4 Faculty of Chemistry, Southern Federal University, 344090 Rostov-on-Don, Russia
5 Institute for Solid State and Material Physics, Technische Universität Dresden, 01069 Dresden, Germany
* Correspondence: vasil@lt.phys.msu.ru

Abstract: Physical properties of the mixed-valent tellurate of lithium and manganese, $LiMn_2TeO_6$, were investigated in measurements of *ac* and *dc* magnetic susceptibility χ, magnetization M, specific heat C_p, electron spin resonance (ESR), and nuclear magnetic resonance (NMR) in the temperature range 2–300 K under magnetic field up to 9 T. The title compound orders magnetically in two steps at T_1 = 20 K and T_2 = 13 K. The intermediate phase at $T_2 < T < T_1$ is fully suppressed by magnetic field $\mu_0 H$ of about 4 T. Besides magnetic phases transitions firmly established in static measurements, relaxation-type phenomena were observed well above magnetic ordering temperature in resonant measurements.

Keywords: manganese oxide; spin order; magnetic phase diagram

check for updates

Citation: Vasilchikova, T.; Vavilova, E.; Salikhov, T.; Nalbandyan, V.; Dengre, S.; Sarkar, R.; Klauss, H.-H.; Vasiliev, A. Static and Resonant Properties and Magnetic Phase Diagram of $LiMn_2TeO_6$. *Materials* **2022**, *15*, 8694. https://doi.org/10.3390/ma15238694

Academic Editors: Musheer Ahmad, Kafeel Ahmad Siddiqui and Mohd Afzal

Received: 21 October 2022
Accepted: 2 December 2022
Published: 6 December 2022

Publisher's Note: MDPI stays neutral with regard to jurisdictional claims in published maps and institutional affiliations.

Copyright: © 2022 by the authors. Licensee MDPI, Basel, Switzerland. This article is an open access article distributed under the terms and conditions of the Creative Commons Attribution (CC BY) license (https://creativecommons.org/licenses/by/4.0/).

1. Introduction

Mixed valence manganese oxides exhibit colossal magnetoresistance effect [1–4] and attract attention as prospective materials in lithium-ion industry [5–8]. Moreover, it has been found that they are capable of strong light adsorption in the solar spectrum range and may serve as magnetic sensors, spintronic, and magnetocaloric devices [9–13]. Along with numerous applications, manganites are quite attractive in fundamental research due to presence of spin, charge, and orbital degrees of freedom often entangled [14–18]. The physics of these systems relates to metal-insulator transition, competing exchange interactions and magnetic frustration [19–22].

In contrast to the widely studied Mn^{3+}/Mn^{4+} mixed-valent oxides, the properties of Mn^{2+}/Mn^{3+} mixed-valent materials are less explored. Although multiple compounds (starting from hausmannite Mn_3O_4) are known to contain simultaneously Mn^{2+} and Mn^{3+}, these cations sit usually on different crystallographic sites and only rarely mix on the same site. Lithium manganese tellurate $Li_2Mn_4Te_2O_{12}$ ($LiMn_2TeO_6$ for short) belongs to this minority [23]. With average oxidation state of 2.5, Mn ions occupy four non-equivalent octahedral positions, but only two of them are definite Mn^{2+} and Mn^{3+}, whereas two others are supposedly mixed Mn^{2+}/Mn^{3+} sites.

Triclinic crystal structure of $LiMn_2TeO_6$ can be considered as a heavily distorted variant of the orthorhombic *Pnn2* structure of Li_2TiTeO_6 [24] with Li/Mn ordering on two independent Li sites. Note that Li_2TiTeO_6 itself is a superstructure derived from $LiSbO_3$ [25]. The differences between these three structures allow considering $LiMn_2TeO_6$ as a new structural type. Ordering of cations may only destroy both glide planes of *Pnn2* structure leading to a monoclinic space group *P112* but not to the triclinic distortion since

all cations in Li_2TiTeO_6 reside on the two-fold axes.The Jahn–Teller effect of Mn^{3+} ions and/or Mn–Mn interactions seem to be the reasons of the triclinic distortion [23].Here, we report a comprehensive study of thermodynamic and magnetic resonance properties of the lithium manganese tellurate $LiMn_2TeO_6$.

2. Experimental

The preparation of $LiMn_2TeO_6$ powder samples by conventional solid-state reaction and their phase analysis, redox analysis, and crystal structure determination have been described in detail earlier [23]. Here, we used samples from the same work, stored in a tightly closed container in a desiccator. Their identity was confirmed by X-ray diffraction. Thermodynamic properties of the title compound, that is the magnetization M and specific heat C_p, were studied using various options of Quantum Design Physical Properties Measurements System PPMS-9T in the temperature range 2–300 K under magnetic field up to 9 T.

The crystal structure of $LiMn_2TeO_6$ [23] contains four different positions of manganese, as shown in Figure 1. One can find planar, chain, and dimer motives in the crystal lattice, but none of them dominates. Therefore, we cannot treat this system as purely two- or one-dimensional. The picture is complicated by the mixed valence of manganese ions. The magnetism relates to a large number of exchange interactions, different in both magnitude and sign: at least one of the bonds has an angle close to 90°, and therefore, is characterized by a ferromagnetic exchange.

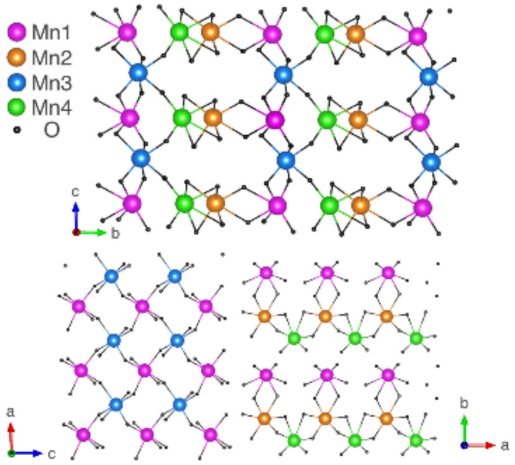

Figure 1. Arrangement of manganese ions in the crystal structure of $LiMn_2TeO_6$ in different planes.

Electron spin resonance (ESR) studies were carried out using an X-band ESR spectrometer "Adani" CMS 8400 ($f \approx 9.4$ GHz, $B \leq 0.7$ T) equipped with a low-temperature mount, operating in the range T = 6–450 K. The effective g-factors have been calculated with respect to an external reference for the resonance field. BDPA with g_{et} = 2.00359 has been used as a reference material.

The ^{7}Li ($I = 3/2$) nuclear magnetic resonance (NMR) spectra were measured using "Tecmag" pulse solid-state NMR spectrometer at various frequencies in the range 10–110 MHz. The NMR spectra were obtained by point-by-point integration of the intensity of the Hahn echo versus magnetic field. The spin-lattice relaxation has been studied by saturation recovery pulse sequence and stimulated echo. In the NMR field sweep spectra, it was not possible to resolve the central line and quadrupole satellites. Thus, the spin-lattice relaxation time T_1 was obtained from the fitting of nuclear spin-echo decay with exponential function.

3. Results and Discussion

3.1. Electron Spin Resonance

In the whole temperature range, a single Lorentzian absorption line has been observed which can be ascribed to overlapping signals from Mn^{2+} and Mn^{3+} ions (Figure 2a). Upon lowering temperature, the signal broadens and eventually disappears below 30 K. Such a signal fading implies proximity to an onset of the long-range antiferromagnetic order and opening of the energy gap for resonance excitations. The main ESR parameters as obtained from fitting in accordance with Lorenzian profile [26] are shown in Figure 2b. The halfwidth ΔB of the ESR signal monotonously broadens with lowering temperature indicating presence of short-range correlation effects in the magnetic subsystem of $LiMn_2TeO_6$. The effective g-factor remains temperature-independent in the range 100–450 K and its value g ~1.98 ± 0.02 is typical for the manganese ions in the high-spin states of Mn^{2+} and Mn^{3+} in octahedral environment. Below 100 K, the effective g-factor deviates from linearity, indicating the effect of short-range magnetic correlations. The temperature dependence of the integral ESR intensity $\chi_{ESR}(T)$ is shown in Figure 3a.

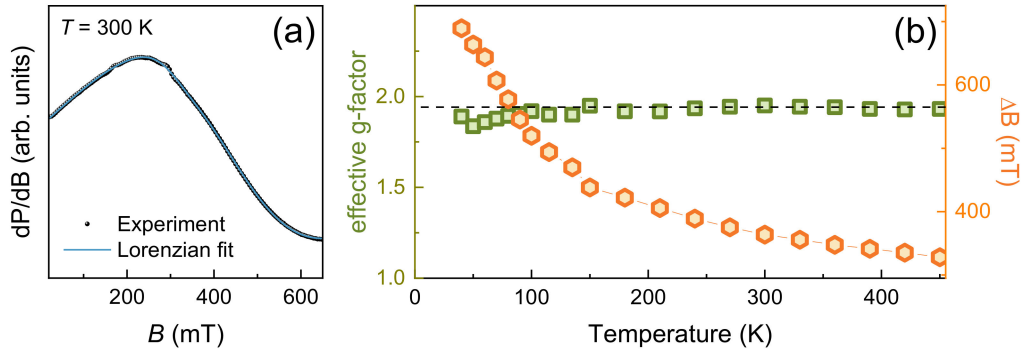

Figure 2. (**a**) ESR spectrum taken at room temperature. (**b**) The temperature dependences of the effective g-factor and ESR linewidth ΔB in $LiMn_2TeO_6$.

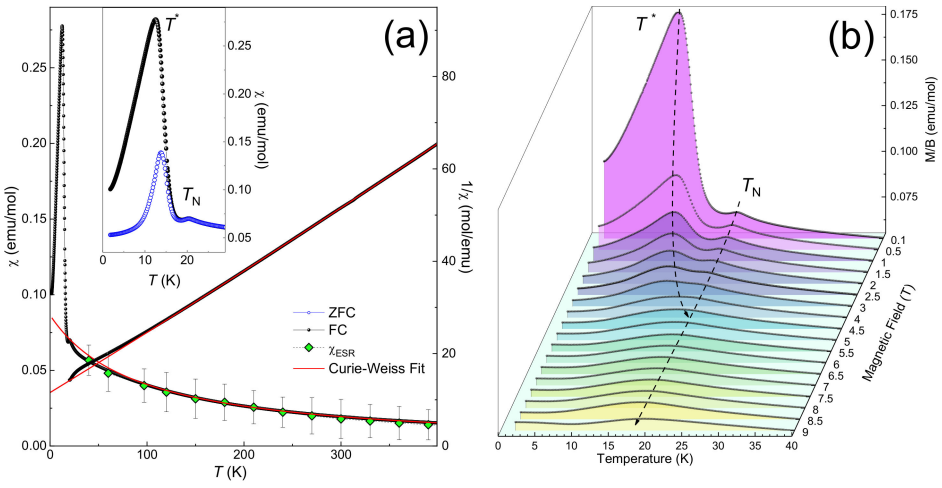

Figure 3. (**a**) The temperature dependences of the magnetic susceptibility recorded in ZFC (blue open symbols) and FC (black sphere) regimes at B = 0.1 T and the integrated ESR intensity (light green diamond) along with inverse magnetic susceptibility $1/\chi$. The red solid line represents an approximation in accordance with the Curie-Weiss law. (**b**) The $M(T)$ curves for the $LiMn_2TeO_6$ taken at various external magnetic fields.

3.2. Magnetization

The temperature dependence of the magnetic susceptibility $\chi = M/B$ in $LiMn_2TeO_6$ is shown in the left panel of Figure 3. At elevated temperatures, the $\chi(T)$ curve follows

the Curie–Weiss law with addition of a temperature-independent term $\chi = \chi_0 + C/(T-\Theta)$, where C = 7.35 emu/mol K is the Curie constant and $\Theta = -95$ K is the Weiss temperature. The diamagnetic term $\chi_0 = -5\times10^{-4}$ emu/mol was found to be in agreement with the sum of Pascal's constants [27] of the ions constituting the $LiMn_2TeO_6$ compound. The negative value of the Weiss temperature indicates the predominance of antiferromagnetic exchange while the value of Curie constant corresponds to a system with equal numbers of Mn^{2+} (spin $S = 5/2$) and Mn^{3+} (spin $S = 2$) ions at averaged g-factor $g = 1.98 \pm 0.02$. Upon decreasing the temperature, the $\chi(T)$ dependence exhibits a sharp maximum at about T_N = 20 K, indicating the long-range antiferromagnetic order. With further cooling, an additional intense peak appears at T^* = 13 K which is sensitive to the measurement protocol, i.e., either zero-field cooling (ZFC) or field cooling (FC) regimes. This fact is illustrated by the inset in Figure 3a.

To further elucidate the magnetic behavior of $LiMn_2TeO_6$ at low temperatures, we measured the $M(T)$ dependences for the $LiMn_2TeO_6$ sample at various magnetic fields up to 9 T, as shown in Figure 3b. Upon increasing the magnetic field, the position of the T^* anomaly noticeably shifts to higher temperature, while the maximum at $T_N$demonstrates the opposite trend. At the field B~ 4 T, both anomalies merge into one phase boundary, and anomaly broadens with increasing external field.

It has been found that magnetization isotherms $M(B)$ display neither hysteresis nor saturation in magnetic fields up to 9 T, as shown in Figure 4. Below T^* ~ 13 K, $M(B)$ curves deviate upward which is expected for the spin-flop transition. Above T^* ~ 13 K, this trend changes to the opposite and $M(B)$ curves deviate downward from linearity.

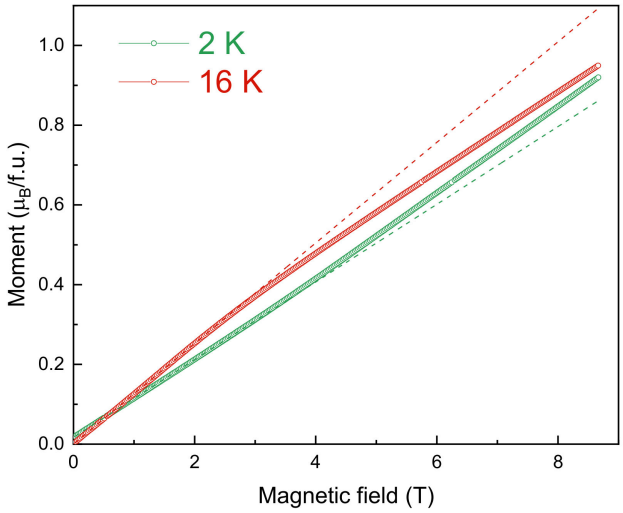

Figure 4. The magnetization isotherms at $T<T_2$ (lower curve) and at $T2 <T<T_1$ in $LiMn_2TeO_6$.

3.3. acMagnetic Susceptibility

ac susceptibility χ_{ac} was measured in the frequency range 0.1–10 kHz. These data are shown in the left panel of Figure 5. The real part of susceptibility χ' shows anomalies at 13 K and 20 K, similar to that found in *dc* magnetization. The behavior of both anomalies differs with the frequency variation. The position of the peak at T_1 = 20 K stays the same while the peak at T_2 = 13 K shifts to higher temperatures with increasing frequency. In the whole temperature range, the imaginary part χ'' is close to zero.

It is worth noting that the behavior of both anomalies with frequency variation is significantly different (inset in Figure 5a). The position of the peak at T_1 remains the same, and this peak can be related to establishment of long-range order. The peak at T_2 is frequency sensitive which is inherent to cluster spin glasses (see Supplementary Materials). The shifts of T_1 and T_2 under external magnetic field agree with static thermodynamic data, as shown in Figure 5b. An increase of the magnetic field above 4 T leads to the shift of the position of the merged anomaly to higher temperatures.

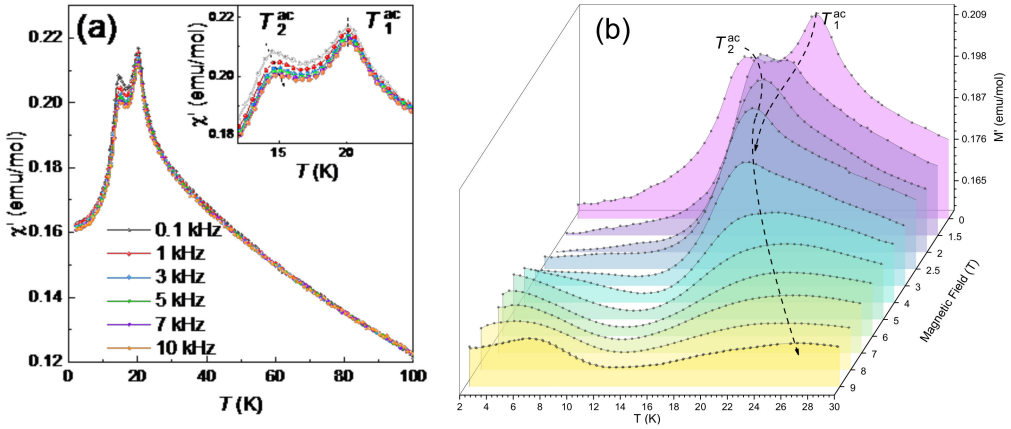

Figure 5. (**a**) Real χ' part of the ac magnetic susceptibility at various frequencies. Inset: the zoomed-in region of real χ' near transitions. (**b**) The temperature dependencies of real part χ' of the *ac* magnetic susceptibility at various magnetic fields at f = 10 kHz.

3.4. Specific Heat

The temperature dependence of specific heat C_p in $LiMn_2TeO_6$ at B = 0 T shown in the left panel of Figure 6 is in good agreement with *dc* magnetic susceptibility measurements showing two distinct anomalies at T_1 and T_2.

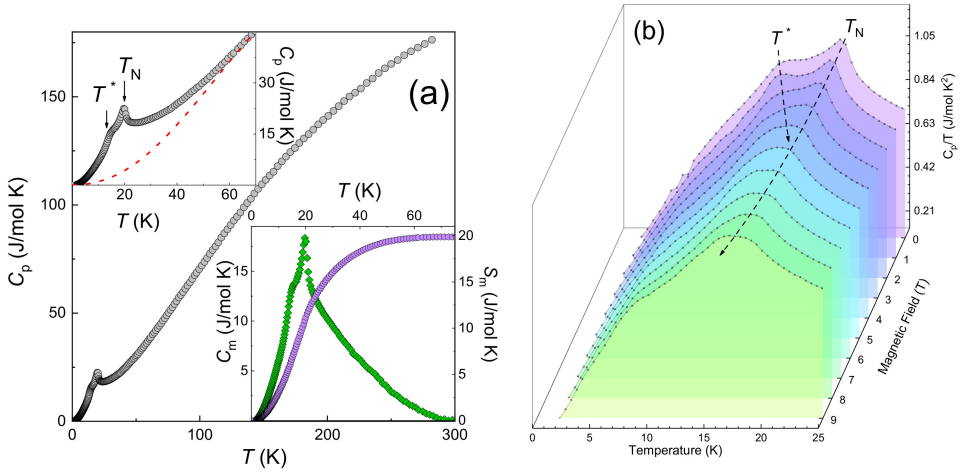

Figure 6. (**a**) Temperature dependence of the specific heat in $LiMn_2TeO_6$ in zero magnetic field. Upper inset highlights the two-step transition at low temperatures. Dash line represents the lattice specific heat within frames of Debye model. Lower inset shows magnetic specific heat C_m(T) and magnetic entropy ΔS_m. (**b**) Temperature dependences of specific heat $C_p(T)$ in $LiMn_2TeO_6$ at various magnetic fields.

The jump of specific heat at T_1 equals ΔC_m = 18.7 J/mol K, as shown in the lower inset to Figure 6a. This value is two times lower than predicted in the mean field theory $\Delta C_{theor} \approx$ 38.8 J/mol K [28]. Magnetic entropy ΔS_m is also shown in this inset. It saturates at ~50 K reaching about 20 J/mol K. This value is again markedly lower than the magnetic entropy change expected from the mean-field theory ΔS_{theor} = 28.3 J/(mol K) [28]. Overall, these data signal the formation of the short-range correlation regime in $LiMn_2TeO_6$ well above the Néel temperature.

The temperature dependences of specific heat $C_p(T)$ taken at various magnetic fields in $LiMn_2TeO_6$ are shown in Figure 6b. As is the case of magnetization measurements, the application of a magnetic field slightly shifts downward the position of anomaly at T_1 and shifts upward the anomaly at T_2.

3.5. Nuclear Magnetic Resonance

To study in detail the low energy spin dynamics at the microscopic level in the region of fraction of micro-eV energy scales, we have carried out ^{7}Li NMR investigations. The crystal structure suggests the presence of Li in two non-equivalent sites in $LiMn_2TeO_6$ with different Mn environments. Therefore, the observed ^{7}Li NMR spectrum is a superposition of the contributions from all lithium nuclei in powder specimen. Insight into the dynamic spin correlations is provided by the ^{7}Li spin-lattice relaxation rate R_1measurements. The low-temperature part of the T-dependence of the spin-lattice relaxation measured in two different external fields is shown in the left panel of Figure 7. The peaks in the temperature dependence of the relaxation correspond to the phase transition temperatures, which is about 18 K at 6.6 T external field, and 20 K at 1.8 T. Above the magnetic phase transition, a critical increase in the relaxation rate is observed, which at 1.8 T is well described by the critical exponent $p \approx 0.48$. This value is close to the predictions of the mean field theory for a three-dimensional magnet [29]. At 6.6 T, an extended region of continuous increase of the relaxation rate with cooling is observed above the peak, indicating development of a very slow dynamics and strong spin correlations.

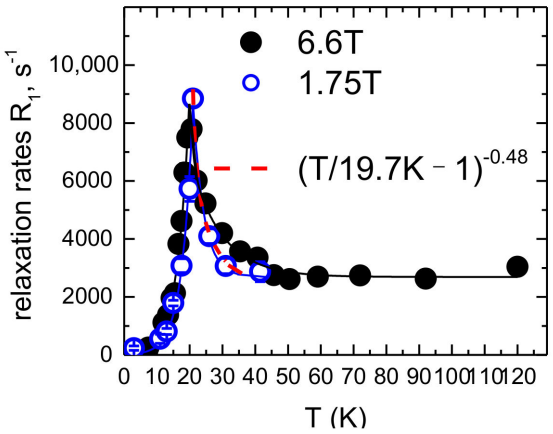

Figure 7. Temperature dependence of the spin-lattice relaxation rate R_1 in $LiMn_2TeO_6$ at two external fields. Solid circles correspond to 6.6 T, open circles to 1.75 T. Dashed line is a critical exponent for 1.75 T (see text).

One can compare the local static and dynamic susceptibility obtained from NMR data with the bulk static susceptibility. The nuclear spin lattice relaxation in magnets is usually governed by magnetic fluctuations in the electronic spin system and R_1T^{-1} is proportional to the imaginary part of the local dynamic susceptibility χ'' [30]:

$$(T_1T)^{-1} \propto \sum_q A_\perp^2\left(\vec{q},\omega\right) \cdot \frac{\chi''\left(\vec{q},\omega\right)}{\omega} \quad (1)$$

Here, A is the q-dependent hyperfine constant, q is the wave vector and ω is the Larmor frequency. As shown in Figure 7, the local dynamic spin susceptibility R_1T^{-1} probed by NMR at the external field of 6.6 T is proportional to the bulk static susceptibility in the temperature range 90–250 K manifesting the paramagnetic regime of the electron spin system. Below 90 K, the dependence deviates from this linearity indicating the slowing down of spin fluctuations and development of correlations.

The establishment of the antiferromagnetic order is reflected in the NMR spectra, which acquire a step-like shape that is specific for powders in such cases. The rectangle components of such a spectrum correspond to magnetically non-equivalent positions of

lithium in an ordered state. The shape of the individual rectangles can be described by the equation [31]:

$$f(H, H_A, H_0) \propto \frac{1}{4H_A}\left|1 + \frac{H_0^2 - H_A^2}{H^2}\right| \quad (2)$$

for $|H_0 - H_A| \leq H \leq H_0 + H_A$. Here, $H_0 = \gamma_n \omega_L$, H_A is a local internal field, ω_L is the paramagnetic Larmor frequency, and γ_n is a nuclear gyromagnetic ratio. For proper interpretation of the results, a correction of the spectrum intensity to the magnitude of the measurement fields was made. The resulting spectra obtained at 12 K are shown in Figure 8 by green color. All spectra contain the narrow gaussian contribution at $H_G = H_0 + 0.11$ T with the width ~0.3 T and the intensity of about 3–4% of total intensity of the spectra (dark grey line) which apparently refers to a small fraction of the diamagnetic impurity.

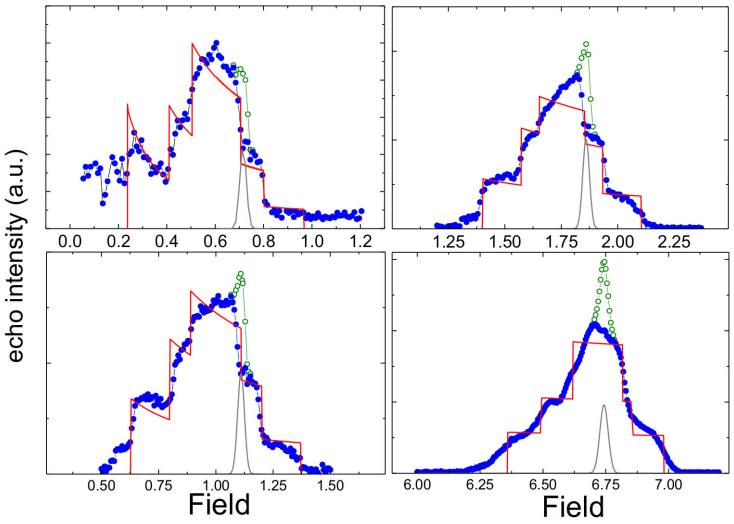

Figure 8. NMR spectra at 12 K obtained in $LiMn_2TeO_6$ under different external field.

Subtracting this Gaussian component from the experimental spectrum, one can obtain the ^{7}Li NMR spectrum in $LiMn_2TeO_6$ (blue line). The modeling of the spectra with the 0.6 T, 1 T, and 1.7 T according to the formula (2) gives almost equal sets of the basic fitting parameters for three different lithium positions: H_0 is a Larmor field, $H_A{}^{(1)} \approx 0.37$ T, $H_A{}^{(2)} \approx 0.185$ T, $H_A{}^{(3)} \approx 0.1$ T and relative intensities $I^{(1)} \approx 50\%$, $I^{(2)} \approx 30\%$, $I^{(3)} \approx 20\%$. The obtained intensity ratio $I^{(1)}/(I^{(2)}+I^{(3)})$ is close to the ratio of the filling of structural positions (Li1:Li2 ~ 5:4). It indicates the appearance of the magnetically nonequivalent atoms in at least one of the structural positions. A strong increase in the external field up to 6.6 T leads to a partial tilting of the manganese spins along the field direction that distorts the shape of the spectrum and, strictly speaking, makes Equation (2) inapplicable. Using it formally, we can get the following simulation parameters: $H_A{}^{(1)} \approx 0.32$ T, $H_A{}^{(2)} \approx 0.175$ T and $H_A{}^{(3)} \approx 0.095$T, $I^{(1)} \approx 50\%$, $I^{(2)} \approx 27\%$, $I^{(3)} \approx 23\%$, but central field of each rectangles is no more $H_0 = 6.648$ T but it shifts steadily to higher values: $H_0{}^{(1)} \approx 6.67$ T, $H_0{}^{(2)} \approx 6.68$ T, and $H_0{}^{(3)} \approx 6.7$ T. Such a different shift of the zero field on different lithium positions indicates the presence of a component of the internal field, collinear to the external one, caused by the tilting of spins in AFM sublattices in a strong external field. The absence of any changes in the spectral shape, except for those caused by gradual tilting of spins in a magnetic field, allows to attribute all these spectra to the same type of magnetic structure and the same magnetic phase.

The temperature transformation of the NMR spectrum in the ordered state obtained at 1.8 T is shown in Figure 9. The shape of the NMR spectrum changes with temperature. The Néel temperature is clearly seen in the line width that dramatically increases below 20K. A pronounced step-like profile is present at temperatures of 12.5 and 10 K. At 15.5 K, the spectrum structure is less resolvable and the width is smaller. At low temperatures, the line

is smoothed, especially on the high-field shoulder, and, at the same time, has a significantly large width.

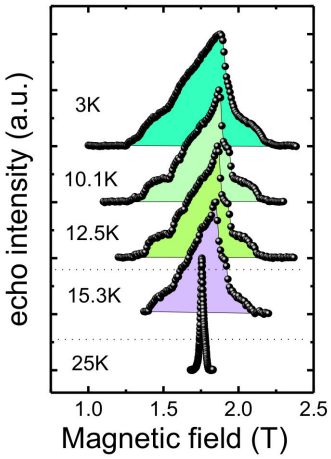

Figure 9. ^{7}Li NMR spectrum for $LiMn_2TeO_6$ at low temperatures in different external field. Dotted lines mark the phase boundaries (see paragraph 4).

4. Discussion

The static magnetic properties of $LiMn_2TeO_6$ are firmly established in measurements of *dc* magnetic susceptibility, magnetization, specific heat. Summarizing the experimental results, the magnetic phase diagram for $LiMn_2TeO_6$ has been established, as shown in Figure 10. At lowering temperature, the title compound orders antiferromagnetically at T_1 = 20 K and experiences second magnetic phase transition at T_2 = 13 K. The intermediate phase at $T_2 < T < T_1$ is fully suppressed by an external magnetic field of 4 T. Such behavior is frequently observed in compounds which experience consecutive incommensurate and commensurate magnetic orders. The antiferromagnetic type of ordering at both $T < T_2$and $T_2 < T < T_1$ is confirmed by the rectangular shape of the ^{7}Li NMR line.

The dynamics of the spin system was examined by NMR and EPR. $LiMn_2TeO_6$ is characterized by an extended region of developed correlations above T_N. X-band ESR signal disappears at about 40 K. Dynamic susceptibility on MHz timescale measured by NMR relaxation rate shows noticeable deviations from the bulk susceptibility below ~50K. Moreover, while the T_1^{-1}(T) dependence obtained at 1.75 T is govern by 3D critical regime in the upper vicinity of T_N, it is not the case at higher magnetic fields. Such behavior proves the development a slow Mn spin correlations well above the ordering temperature. Usually if the correlations in a magnetic system slow down with decreasing temperature, it is usually followed, almost immediately, by a static ordered or glassy regime. The wide temperature range of slow and not three-dimensional correlations indicates that magnetism of $LiMn_2TeO_6$is determined by a complex network of Mn^{3+} and Mn^{4+} exchange interactions which are of different magnitude and partially frustrated. The competition of these interactions apparently causes the appearance of an intermediate phase below the Néel temperature.

It could be of interest to compare physical properties of $LiMn_2TeO_6$ with those of its iso-elemental counterpart Li_2MnTeO_6 [22]. While the magnetic susceptibility of Li_2MnTeO_6 shows no obvious anomaly indicative of a long-range magnetic order at low magnetic fields, at high magnetic field it evidences the antiferromagnetic-type peak at about 9 K confirmed also by specific heat measurements. Furthermore, this conclusion is supported also by ^{7}Li NMR data and dielectric permittivity measurements. Density functional theory calculations lead to a 120° noncollinear spin arrangement which agrees with the magnetic structure defined in neutron-diffraction measurements.

Despite similar chemical compositions of $LiMn_2TeO_6$ and Li_2MnTeO_6, their physical properties differ drastically due the difference of oxidation states, i.e., Mn^{2+}/Mn^{3+} in the

former compound and Mn^{4+} in the latter compound. Mixed valence of manganese results in the appearance of ferromagnetic double exchange on the background of antiferromagnetic superexchange in $LiMn_2TeO_6$ to be compared with purely antiferromagnetic exchange in Li_2MnTeO_6.

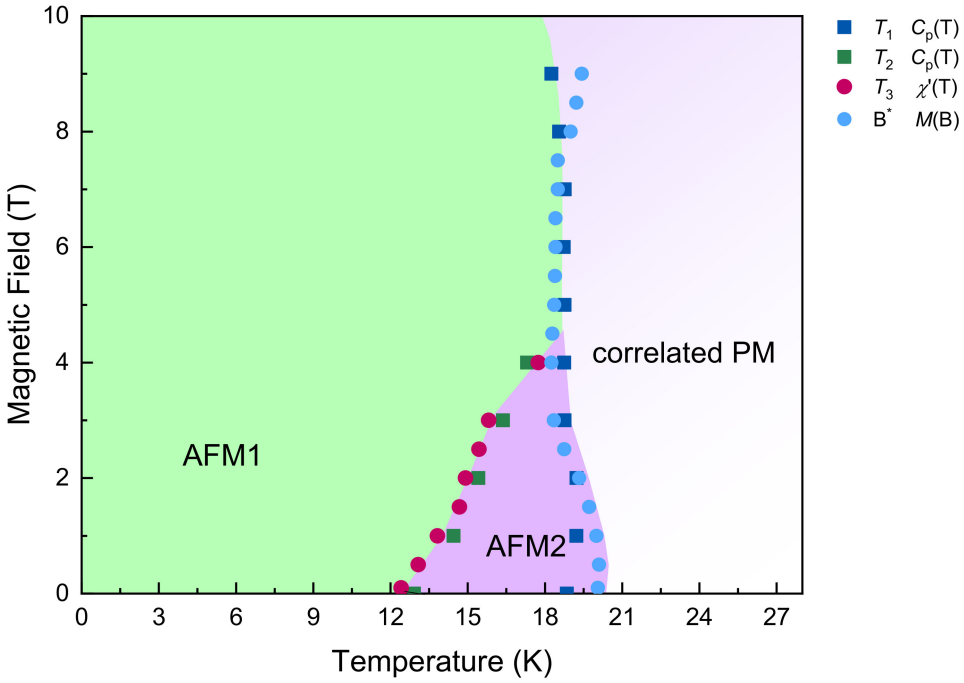

Figure 10. The magnetic phase diagram for tellurate $LiMn_2TeO_6$.

5. Summary

Summarizing, the competition of various exchange interactions and the presence of both divalent and trivalent manganese ions in $LiMn_2TeO_6$ leads to the two-step formation of antiferromagnetic state at T_1 = 20 K and T_2 = 13 K. The phase at $T_2 < T < T_1$ is readily suppressed by an external magnetic field $\mu_0 H$ of 4 T. At high fields, well above the Néel temperature, an extended correlation region is found, characterized by large correlation time. It can be explained by the multicomponent nature of the magnetic system, which has a complicated geometry and is partially frustrated.

Supplementary Materials: The following supporting information can be downloaded at: https://www.mdpi.com/article/10.3390/ma15238694/s1, Figure S1: Critical slowing down behavior of the peak position Tf.; Figure S2: 7Li NMR spectrum for LiMn2TeO6 at different temperatures in low and high external fields.

Author Contributions: Conceptualization, E.V. and H.-H.K.; Methodology, T.V., T.S., V.N. and S.D.; Validation, V.N. and R.S.; Formal analysis, H.-H.K.; Investigation, T.V., E.V., T.S., S.D. and R.S.; Writing—review & editing, A.V.; Supervision, A.V. All authors have read and agreed to the published version of the manuscript.

Funding: This project was initially developed by Elena Zvereva who passed away early in 2021. A part of the thermodynamic data presented in this paper were obtained by Elena. This research has been supported by the Megagrant program of the Government of Russian Federation through the project 075-15-2021-604. E.V. and T.S would like to thank the financial support from the government assignment for FRC Kazan scientific Center of RAS.

Institutional Review Board Statement: Not applicable.

Informed Consent Statement: Not applicable.

Data Availability Statement: Not applicable.

Acknowledgments: This project was initially developed by Elena Zvereva who passed away early in 2021. A part of the thermodynamic data presented in this paper were obtained by Elena. This research has been supported by the Megagrant program of the Government of Russian Federation through the project 075-15-2021-604. E.V. and T.S would like to thank the financial support from the government assignment for FRC Kazan scientific Center of RAS. Magnetic studies by T.V. were support by Russian Scientific Foundation through Grant No. 22-42-08002.

Conflicts of Interest: The authors declare no conflict of interest.

References

1. Bebenin, N.G.; Zainullina, R.I.; Ustinov, V.V. Colossal magnetoresistance manganites. *Phys. -Uspekhi* **2018**, *61*, 719–738. [CrossRef]
2. Wagner, P.; Wackers, G.; Cardinaletti, I.; Manca, J.; Vanacken, J. From colossal magnetoresistance to solar cells: An overview on 66 years of research into perovskites. *Phys. Status Solidi A* **2017**, *214*, 1700394. [CrossRef]
3. Raveau, B. The crucial role of mixed valence in the magnetoresistance properties of manganites and cobaltites. *Phil. Trans. R Soc. A* **2008**, *366*, 83–92. [CrossRef] [PubMed]
4. Şen, C.; Alvarez, G.; Dagotto, E. Competing Ferromagnetic and Charge-Ordered States in Models for Manganites: The Origin of the Colossal Magnetoresistance Effect. *Phys. Rev. Lett.* **2007**, *98*, 127202. [CrossRef] [PubMed]
5. Armstrong, A.R.; Bruce, P.G. Synthesis of layered $LiMnO_2$ as an electrode for rechargeable lithium batteries. *Nature* **1996**, *381*, 499–500. [CrossRef]
6. Huang, Y.; Dong, Y.; Li, S.; Lee, J.; Wang, C.; Zhu, Z.; Xue, W.; Li, Y.; Li, J. Lithium Manganese Spinel Cathodes for Lithium-Ion Batteries. *Adv. Energy Mater.* **2021**, *11*, 2000997. [CrossRef]
7. Thackeray, M.M.; Lee, E.; Shi, B.; Croy, J.R. Review–From $LiMn_2O_4$ to Partially-Disordered Li_2MnNiO_4: The Evolution of Lithiated-Spinel Cathodes for Li-Ion Batteries. *J. Electrochem. Soc.* **2022**, *169*, 020535. [CrossRef]
8. Liu, S.; Wang, B.; Zhang, X.; Zhao, S.; Zhang, Z.; Yu, H. Reviving the lithium-manganese-based layered oxide cathodes for lithium-ion batteries. *Matter* **2021**, *4*, 1511–1527. [CrossRef]
9. Wolf, S.A.; Awschalom, D.D.; Buhrman, R.A.; Daughton, J.M.; von Molnár, S.; Roukes, M.L.; Chtchelkanova, A.Y.; Treger, D.M. Spintronics: A Spin-Based Electronics Vision for the Future. *Science* **2001**, *294*, 1488–1495. [CrossRef]
10. Yang, Q.; Yao, J.; Zhang, K.; Wang, W.; Zuo, X.; Tang, H.; Wu, M.; Li, G. Perovskite-type $La_{1-x}Ca_xMnO_3$ manganese oxides as effective counter electrodes for dye-sensitized solar cells. *J. Electroanalyt. Chem.* **2019**, *833*, 1–8. [CrossRef]
11. Gager, E.; Frye, M.; McCord, D.; Scheffe, J.C.; Nino, J. Reticulated porous lanthanum strontium manganite structures for solar thermochemical hydrogen production. *Int. J. Hydrog. Energy* **2022**, *47*, 31152–31164. [CrossRef]
12. Riaz, A.; Kreider, P.; Kremer, F.; Tabassum, H.; Yeoh, J.S.; Lipiński, W.; Lowe, A. Electrospun Manganese-Based Perovskites as Efficient Oxygen Exchange Redox Materials for Improved Solar Thermochemical CO_2 Splitting. *ACS Appl. Energy Mater.* **2019**, *2*, 2494–2505. [CrossRef]
13. Sánchez-Ochoa, F.; Springborg, M. Silver hollandite ($Ag_xMn_8O_{16}$, x < 2): A highly anisotropic half-metal for spintronics. *Phys. Rev. Mat.* **2021**, *5*, 095001. [CrossRef]
14. Prodi, A.; Gilioli, E.; Gauzzi, A.; Licci, F.; Marezio, M.; Bolzoni, F.; Huang, Q.; Santoro, A.; Lynn, J.W. Charge, orbital and spin ordering phenomena in the mixed valence manganite $(NaMn^{3+}{}_3)(Mn^{3+}{}_2Mn^{4+}{}_2)O_{12}$. *Nat. Mater.* **2004**, *3*, 48–52. [CrossRef]
15. Coey, M. Charge-ordering in oxides. *Nature* **2004**, *430*, 155–157. [CrossRef]
16. Qiu, X.; Proffen, T.; Mitchell, J.F.; Billinge, S.J.L. Orbital Correlations in the Pseudocubic O and Rhombohedral R Phases of $LaMnO_3$. *Phys. Rev. Lett.* **2005**, *94*, 177203. [CrossRef]
17. Johnson, R.D.; Mezzadri, F.; Manuel, P.; Khalyavin, D.D.; Gilioli, E.; Radaelli, P.G. Evolution of Magneto-Orbital order Upon B-Site Electron Doping in $Na_{1-x}Ca_xMn_7O_{12}$ Quadruple Perovskite Manganites. *Phys. Rev. Lett.* **2018**, *120*, 257202. [CrossRef]
18. Volkova, O.S.; Shvanskaya, L.V.; Ovchenkov, E.A.; Zvereva, E.A.; Volkov, A.S.; Chareev, D.A.; Molla, K.; Rahaman, B.; Saha-Dasgupta, T.; Vasiliev, A.N. Structure–Property Relationships in α-, β′-, and γ-Modifications of $Mn_3(PO_4)_2$. *Inorg. Chem.* **2016**, *55*, 10692–10700. [CrossRef]
19. Ederer, C.; Spaldin, N.A. A new route to magnetic ferroelectrics. *Nat. Mater.* **2004**, *3*, 849–851. [CrossRef]
20. Rairigh, R.P.; Singh-Bhalla, G.; Tongay, S.; Dhakal, T.; Biswas, A.; Hebard, A.F. Colossal magnetocapacitance and scale-invariant dielectric response in phase-separated manganites. *Nat. Phys.* **2007**, *3*, 551–555. [CrossRef]
21. Kurbakov, A.I.; Susloparova, A.E.; Pomjakushin, V.Y.; Skourski, Y.; Vavilova, E.L.; Vasilchikova, T.M.; Raganyan, G.V.; Vasiliev, A.N. Commensurate helicoidal order in the triangular layered magnet Na_2MnTeO_6. *Phys. Rev. B* **2022**, *105*, 064416. [CrossRef]
22. Zvereva, E.A.; Raganyan, G.V.; Vasilchikova, T.M.; Nalbandyan, V.B.; Gafurov, D.A.; Vavilova, E.L.; Zakharov, K.V.; Koo, H.-J.; Pomjakushin, V.Y.; Susloparova, A.E.; et al. Hidden magnetic order in the triangular-lattice magnet Li_2MnTeO_6. *Phys. Rev. B* **2020**, *102*, 094433. [CrossRef]
23. Pospelov, A.A.; Nalbandyan, V.B.; Serikova, E.I.; Medvedev, B.S.; Evstigneeva, M.A.; Ni, E.V.; Lukov, V.V. Crystal structure and properties of a new mixed-valence compound $LiMn_2TeO_6$ and the survey of the $LiMM'XO_6$ family (X = Sb or Te). *Solid State Sci.* **2011**, *13*, 1931–1937. [CrossRef]
24. Choisnet, A.J.; Rulmont, A.; Tarte, P. Ordering phenomena in the $LiSbO_3$ type structure: The new mixed tellurates Li_2TiTeO_6 and Li_2SnTeO_6. *J. Solid State Chem.* **1989**, *82*, 272–278. [CrossRef]

25. Genkina, E.A. Accurate definition of $LiSbO_3$ crystal structure. *Kristallografiya* **1992**, *37*, 356–358.
26. Ivanshin, V.A.; Deisenhofer, J.; Krug von Nidda, H.-A.; Loidl, A.; Mukhin, A.; Balbashov, J.; Eremin, M.V. ESR study in lightly doped $La_{1-x}Sr_xMnO_3$. *Phys. Rev. B: Cond. Matter Mater. Phys.* **2000**, *61*, 6213–6219. [CrossRef]
27. Bain, G.A.; Berry, J.F. Diamagnetic Corrections and Pascal's Constants. *J. Chem. Educ.* **2008**, *85*, 532–536. [CrossRef]
28. Tari, A. *The Specific Heat of Matter at Low Temperatures*; Imperial College Press: London, UK, 2003.
29. Stanley, H.E. *Introduction to Phase Transitions and Critical Phenomena*; Oxford University Press: Oxford, UK, 1987.
30. Moriya, T. The Effect of Electron-Electron Interaction on the Nuclear Spin Relaxation in Metals. *J. Phys. Soc. Jpn.* **1963**, *18*, 516–520. [CrossRef]
31. Yamada, Y.; Sakata, A. An Analysis Method of Antiferromagnetic Powder Patterns in Spin-Echo NMR under External Fields. *J. Phys. Soc. Jpn.* **1986**, *55*, 1751–1758. [CrossRef]